Journal of The Electrochemical Society, **164** (2) F171-F179 (2017)
0013-4651/2017/164(2)/F171/9/$37.00 © The Electrochemical Society

Modeling of Transient Platinum Degradation in a Low Pt-Loading PEFC under Current Cycling

Yubai Li* and **C.Y. Wang****,z

Department of Mechanical and Nuclear Engineering, and Electrochemical Engine Center (ECEC), The Pennsylvania State University, University Park, Pennsylvania 16802, USA

Pt degradation is one of the most important aging mechanisms that control the lifespan of automotive polymer electrolyte fuel cells (PEFCs). The consequence of Pt degradation is loss of the electrochemical active surface area (ECA) in cathode catalyst layers (CCLs) of PEFCs. The reduction of ECA increases not only the activation overpotential through reducing sites of oxygen reduction reaction (ORR) kinetics but also the mass transport loss through causing an additional micro-scale oxygen transport resistance in the ionomer film surrounding Pt particles. In this study, a 1D physics-based Pt degradation submodel is coupled into the transient M2 model to study the non-uniform Pt degradation and its impacts on long-term PEFC performance. The performance loss of a low Pt-loading PEFC with Pt degradation, the interactions of Pt degradation with the micro-scale transport resistance, the cause and consequence of non-uniform Pt degradation, as well as a strategy of raising lower current density in current cycling test are quantified. This Pt degradation model is demonstrated to be an effective approach to better understand Pt degradation, performance loss caused by Pt degradation, and mitigation strategies to alleviate Pt degradation, all important for achieving excellent durability of PEFCs.

Manuscript submitted November 17, 2016; revised manuscript received December 19, 2016. Published January 19, 2017.

Cost and durability are the two most critical challenges faced in emerging commercial applications of PEFCs, especially for PEFCs in automotive applications.[1] Pt catalysts at the CCL play an important role in PEFCs from both cost and durability points of view. Due to the sluggish ORR at CCL, sufficient Pt catalysts are needed at CCL to provide ECA for the ORR kinetics. The cost of these Pt catalysts could not be reduced by mass production and features largely in the total cost of PEFC stacks. In addition, recent studies found a micro-scale oxygen transport resistance through the ionomer film covering the Pt nanoparticles.[2–5] It is found that this micro-scale resistance increases with ECA normalized current density.[6,7] This means under low Pt-loading condition, this micro-scale resistance will cause high voltage loss at large current density and governs the limiting current density. Thus, although significant reduction of Pt loading at PEFC CCL has been achieved over the last several decades,[8] the barrier of the micro-scale resistance impedes further reduction of Pt loading.

At the same time, the Pt catalysts in the form of nanoparticles inevitably degrade under dynamic load condition of automotive PEFCs.[9–11] Pt nanoparticles are prone to dissolution when the CCL is subjected to high voltage, as their small diameter results in higher Gibbs-Thomson energy.[12] The Pt dissolution phenomenon is the driving force of Pt Ostwald ripening and Pt dissolution and re-precipitation in non-conductive ionomer phase.[13] This Pt degradation is found to be significantly enhanced under voltage cycling condition.[14–18] For automotive PEFCs, the load ramps up and down at acceleration and deceleration, which means the PEFCs work under dynamic voltage condition. The dynamic load induced Pt degradation is found to be one of the most important degradation mechanisms for automotive PEFCs.[11] The consequence of Pt degradation is the loss of valuable ECA in CCL. For the low Pt-loading CCL especially, the loss of ECA will not only induce ORR kinetic losses, but also cause extra voltage loss by increasing the micro-scale transport resistance. Clearly, modeling the Pt degradation in PEFC CCLs and the performance of PEFCs after degradation is sorely needed to estimate long-term performance and to find methods to mitigate Pt degradation.

Due to the vital role of PEFC CCL, extensive modeling studies have been performed from macroscale to pore scale regarding the transport phenomenon and performance of CCL.[19,20] The homogeneous model[21,22] and agglomerate model[4,23–28] are two prevalent macroscale models established for PEFC CCL. In the agglomerate model, the CCL is assumed to be composed by agglomerates which are clusters of carbon particles with Pt catalysts on their surface, ionomer and pores. Typically the macroscale PEFC CCL modeling is a part of macroscale PEFC dynamic modeling,[29–33] which has become an essential approach in current PEFC design.[34–37] On the other hand, Wang et al.[38] developed a pore scale modeling method for PEFC electrodes by using direct numerical simulation (DNS) method. With this pore scale model, the morphology effects on CCL performance were investigated and optimal volume fractions of the void and electrolyte phases were predicted in a subsequent study.[39] Lange et al.[40] developed pore scale modeling and performed modeling with stochastically reconstructed microstructures. The impacts of the carbon particle radius on Knudsen diffusion, proton conductivity and oxygen consumption were investigated with this model. The effects of water vapor transport and thermal transport were then studied with this pore scale CCL modeling method.[41] The up-to-date understanding of PEFC CCL and parameters adjusted by experimental measurement or the pore scale CCL modeling study[42] could provide valuable input into macroscale PEFC CCL modeling. For example, Hao et al.[43] integrated the micro-scale oxygen transport resistance[6] into a comprehensive PEFC model, M2 model, to capture the low CCL Pt-loading effect on PEFC performance, and extended the M2 model capability to model low Pt-loading PEFCs. The agglomeration effect is specifically discussed in their study and this low Pt-loading PEFC model was systematically validated with experimental data under a wide range of Pt loading.[43]

Mathematical modeling of Pt degradation has been performed to elucidate the fundamental mechanisms of Pt degradation in PEFC CCLs.[44–56] Darling and Meyers[44] set up a kinetic model to describe Pt nanoparticle oxidation and dissolution reactions in PEFC CCLs. The model was applied to study the effects of the electrode potential and particle size on rate of Pt degradation.[44] Bi and Fuller[47] then developed a physics-based 1D Pt degradation model and assumed a simplified bi-modal particle size distribution (PSD) for Pt particles. The Pt Ostwald ripening and Pt dissolution-re-precipitation mechanisms were investigated in their study. In a recent study, Holby and Morgan[50] applied much finer Pt particle size bins in their Pt degradation model and specifically discussed the impacts of the Pt PSD shape on the speed of Pt degradation. Based on the kinetic equations developed by Holby and Morgan,[50] Li et al.[53] developed a 1D Pt degradation model to investigate the non-uniform Pt degradation and predict the non-uniform ECA loss across the CCL. The overall ECA evolutions and PSDs at various positions of CCL were compared with experimental data in their study.[53] The 1D Pt degradation model of Li et al.[53] describes the Ostwald ripening and Pt dissolution-re-precipitation across the CCL, which is similar to the Pt degradation model proposed by Takeshita et al.[54] However, by incorporating the temperature-dependent kinetic equations of Holby and Morgan[50] and developing an additional

*Electrochemical Society Student Member.
**Electrochemical Society Member.
zE-mail: cxw31@psu.edu

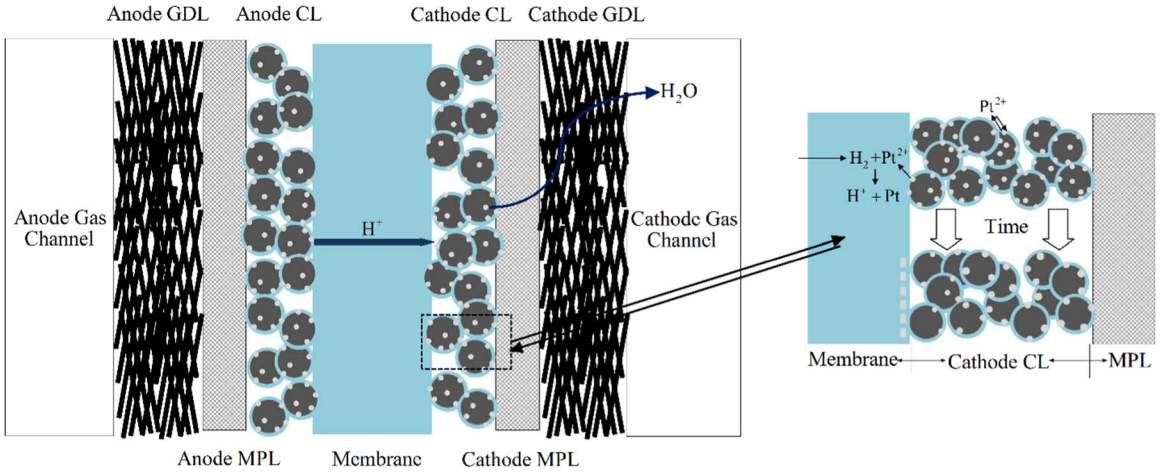

Figure 1. Schematic of coupling Pt degradation model into M2 model.

correlation accounting for the humidity effect on Pt degradation, this model can evaluate the Pt degradation process under various temperatures and RHs. Nonetheless, this Pt degradation model neglects the agglomeration effect as most models of catalyst degradation did.[55]

The non-uniform Pt degradation causes non-uniform ECA across the PEFC CCL in the through-plane direction as introduced. This non-uniform ECA distribution of the degraded PEFC CCL could reshape the current density distributions in PEFC CCLs. Jomori et al.[57] established a 1D PEFC model with the micro-scale oxygen transport submodel implemented to investigate PEFCs with low Pt-loadings. A 1D non-uniform ECA profile across the CCL was assumed and incorporated into their model to reveal how the non-uniform Pt degradation reshapes the current density distribution in the through-plane direction across CCL and to evaluate the performance of the non-uniform degraded low Pt-loading PEFCs.[57] The non-uniform Pt degradation phenomenon is not limited to the through-plane direction, as Pt degradation is faster under higher temperature and higher relative humidity (RH).[58] Due to the complex water and thermal transport phenomenon in PEFCs, the humidity and temperature are highly non-uniform in PEFC CCLs, in the channel-land dimension for example.[59] In this paper, a transient PEFC model coupling the Pt degradation modeling and the Pt performance modeling is established by implementing the 1D physics-based Pt degradation model[53] into the M2 model with low Pt-loading CCL effects considered.[43]

Our primary objective of this work is to numerically evaluate the in-plane distribution of Pt degradation between land and channel areas such that one can assess how much effect the land-to-channel width ratio is on not only fuel cell performance but also durability. Similarly for future work, one can develop a combined model of Pt degradation with a 2D (in the through-plane and along-channel directions) M2 transport model to assess any potential effects of dry-wet transition and co-/counter-flow on fuel cell durability.

Numerical Modeling

The schematic of coupling Pt degradation model as a submodel in the CCL domain into the M2 model in all PEFC domains is shown in Figure 1. With this model, the impacts of the Pt degradation on the low Pt-loading PEFC performance and on the reaction current distribution in PEFC CCLs are investigated. Although the current stage of study considers Pt nanoparticles as catalyst for PEFCs, the methodology used in this study could be extended to explore degradation and performance of PEFC CCL with Pt alloys or alternative metal content as catalysts, which both receive much research to date.[60–63]

Transient M2 model.—In this study, a 1D physics-based Pt degradation model is integrated into the transient M2 model with the low Pt-loading effects in consideration. For the transient M2 model, conservation equations of mass, momentum, species and charge are solved and these equations can be expressed as:

Continuity equation:

$$\nabla \cdot (\rho \vec{u}) = 0 \quad [1]$$

Momentum conservation:

$$\frac{\rho}{\varepsilon}\left[\frac{\partial \vec{u}}{\partial t} + \frac{1}{\varepsilon}\nabla \cdot (\vec{u}\vec{u})\right] = -\nabla p + \nabla \cdot \tau + S_u \quad [2]$$

Energy conservation:

$$\frac{\partial \left(\rho c_p T\right)}{\partial t} + \nabla \cdot \left(\gamma_T \rho c_p \vec{u} T\right) = \nabla \cdot \left(k^{\text{eff}} \nabla T\right) + S_T \quad [3]$$

Species conservation:

$$\varepsilon^{\text{eff}} \frac{\partial C^{\text{k}}}{\partial t} + \nabla \cdot \left(\gamma_c \vec{u} C^{\text{k}}\right) = \nabla \cdot \left(D_{\text{g}}^{\text{k,eff}} \nabla C_{\text{g}}^{\text{k}}\right) - \nabla \cdot \left[\left(\frac{m f_{\text{l}}^{\text{k}}}{M^{\text{k}}} - \frac{C_{\text{g}}^{\text{k}}}{\rho_{\text{g}}}\right) \vec{j}_{\text{l}}\right] + S_{\text{k}} \quad [4]$$

Charge conservation (electrons):

$$0 = \nabla \cdot \left(\sigma^{\text{eff}} \nabla \Phi_{\text{s}}\right) + S_{\Phi_{\text{s}}} \quad [5]$$

Charge conservation (protons):

$$0 = \nabla \cdot \left(\kappa^{\text{eff}} \nabla \Phi_{\text{e}}\right) + S_{\Phi_{\text{e}}} \quad [6]$$

where ρ,$\vec{u}$, P, T, C^{k}, Φ_{s} and Φ_{e} are the density, superficial velocity, pressure, temperature, species molar concentration, electronic and electrolyte phase potential. The source terms for these conservation equations may be found in Reference 64. To reduce the computational time and the mesh for this full physic based transient modeling, a 2D differential cell is used in the present study as illustrated in Figure 2. As shown in Figure 2, the 1D physics-based Pt degradation model is implemented at the nodes of CCL in transient M2 model. The important geometric and physical properties used in the transient M2 model can be found in Table I.

Pt degradation model.—In the physics-based Pt degradation model, the electrochemical reactions of Pt nanoparticle oxidation and dissolution are modeled. In the 1D Pt degradation model, at each control volume i, a certain number of discrete particle size groups are assigned. The particle size group number at each control volume is denoted by j. The Pt nanoparticle diameter $d_{\text{i,j}}$ and the Pt oxide coverage $\theta_{\text{i,j}}$ in each particle size group at every control volume are tracked

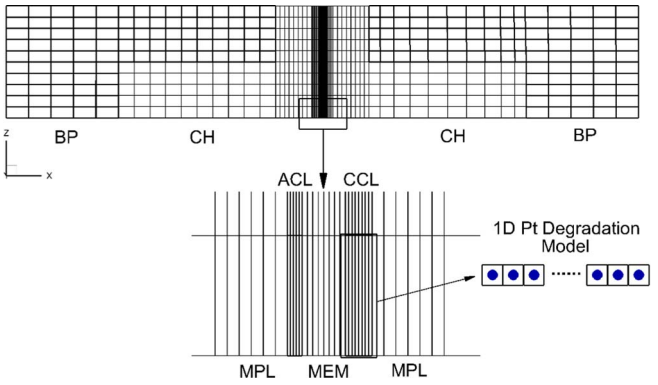

Figure 2. Geometry, computational mesh and 1D Pt degradation coupling scheme.

in the 1D degradation model by solving:[50]

$$\frac{d(d_{\mathrm{i,j}})}{dt} = -r_{net,Pt}\,\Omega \qquad [7]$$

$$\frac{d(\theta_{\mathrm{i,j}})}{dt} = \frac{r_{net,oxide}}{\Gamma} - \frac{2\theta_{\mathrm{i,j}}}{d_{\mathrm{i,j}}}\frac{d(d_{\mathrm{i,j}})}{dt} \qquad [8]$$

where Ω is molar volume of Pt. While the Pt particle net oxidation rate $r_{net,oxide}$ and the net Pt dissolution rate $r_{net,Pt}$ can be expressed as:[50]

$$r_{net,oxide} = \nu_1^*\Gamma \exp\left[\frac{-1}{RT}\left(\bar{H}_{2,fit} + \Lambda\theta_{\mathrm{i,j}}\right)\right] \times \begin{pmatrix} \left(1 - \frac{\theta_{\mathrm{i,j}}}{2}\right)\exp\left[-\frac{nF(1-\beta_2)}{RT}\left(U_{fit} + \frac{\omega\theta_{\mathrm{i,j}}}{nF} - \Delta\Phi\right)\right] \\ -\frac{\nu_2^*}{\nu_1^*}\exp\left[\frac{nF\beta_2}{RT}\left(U_{fit} + \frac{\omega\theta_{\mathrm{i,j}}}{nF} - \Delta\Phi\right)\right] \end{pmatrix} \qquad [9]$$

Table I. Geometrical and physical parameters.

Quantity	Value
Gas channel depth/width	0.7/0.5 mm
Shoulder width	0.5 mm
GDL thickness	160 μm
MPL thickness	30 μm
ACL/CCL thickness	6/11 μm
Membrane thickness	18 μm
Porosity of GDLs/ MPLs	0.625/0.5
Weight ratio of ionomer to carbon in ACL/CCL	0.6/0.95
Equivalent weight of dry membrane	950 g/mol
Dry density of membrane	1.9 g/cm^3
Carbon support density	1.95 g/cm^3
Thermal conductivity of the membrane	0.95 W/m K
Thermal conductivity of the catalyst layer	1.0 W/m K
Thermal conductivity of the GDLs/MPLs through plane direction	0.5/0.3 W/m K
Thermal conductivity of GDLs/MPLs in plane direction	20.0/5.0 W/m K
Hydraulic permeability of MPLs /CLs	8.0×10^{-14} /8.0×10^{-14} m^2
Hydraulic permeability of GDLs through plane direction	1.5×10^{-11} m^2
Hydraulic permeability of GDLs in plane direction	8.0×10^{-12} m^2
Surface tension, liquid-water-air (80°C)	0.0625 N/m
Contact angle in GDLs/ MPLs/CLs	120°, 130°, 100°

Table II. Physical properties for Pt degradation modeling.

Quantity	Value
Reference Pt^{2+} concentration, $c^{ref}_{Pt^{2+}}$	4.0×10^{-3} mol/L
Pt dissolution activation enthalpy under fully humidified condition, $\bar{H}_{1,fit,100\%RH}$	4.0×10^4J/mol
Partial molar oxide formation activation enthalpy(zero coverage),[50] $\bar{H}_{2,fit}$	1.2×10^4 J/mol
Pt oxide formation bulk equilibrium voltage,[50] U_{fit}	1.03 V
Pt dissolution bulk equilibrium voltage,[50] U_{eq}	1.188 V
Butler-Volmer transfer coefficient for Pt dissolution,[50] β_1	0.5
Butler-Volmer transfer coefficient for Pt oxide formation,[50] β_2	0.5
Pt surface site density,[50] Γ	2.2×10^{-9} mol/cm^2
Pt [1 1 1] surface tension,[50] γ	2.4×10^{-4}J/cm^2
Pt oxide dependent kinetic barrier constant,[50] Λ	2.0×10^4J/mol
Dissolution attempt frequency,[50] ν_1	1×10^4 Hz
Backward dissolution rate factor,[50] ν_2	8×10^5 Hz
Forward Pt oxide formation rate constant,[50] ν_1^*	1×10^4 Hz
Backward Pt oxide formation rate constant,[50] ν_2^*	2×10^{-2} Hz
Pt oxide-oxide interaction energy,[50] ω	5.0×10^4 J/mol
Initial average Pt particle diameter	2.59 nm
Variance of initial Pt particle diameter distribution (Gauss)	0.22

$$r_{net,Pt} = \nu_1\Gamma \exp\left[\frac{-\bar{H}_{1,fit}}{RT}\right]\left(1 - \min(1, \theta_{\mathrm{i,j}})\right) \times \begin{pmatrix} \exp\left[-\frac{nF(1-\beta_1)}{RT}\left(U_{eq} - \frac{4\Omega\gamma_{total}}{d_{\mathrm{i,j}}nF} - \Delta\Phi\right)\right] \\ -\frac{\nu_2}{\nu_1}\frac{c_{Pt^{2+}}}{c^{ref}_{Pt^{2+}}}\exp\left[\frac{nF\beta_1}{RT}\left(U_{eq} - \frac{4\Omega\gamma_{total}}{d_{\mathrm{i,j}}nF} - \Delta\Phi\right)\right] \end{pmatrix} \qquad [10]$$

In these expressions, $\Delta\Phi$ is the local difference of the electronic potential and ionomer phase potential $\Phi_s - \Phi_e$ from transient M2 modeling. $c_{Pt^{2+}}$ is solved from 1D Pt ion diffusion equation at each time step of the transient Pt degradation modeling.[53] The temperature T is the temperature field in CCL solved by M2 model. A correlation of $\bar{H}_{1,fit}$ with the water activity in CCL[53] is used in this model to capture the humidity effect on Pt degradation:

$$\bar{H}_{1,fit} = \bar{H}_{1,fit,100\%RH}\left[0.3\,(1-a) + 1\right] \qquad [11]$$

The physical parameters used in Pt degradation model are listed in Table II. By tracking the evolution of $d_{\mathrm{i,j}}$ in every particle size group, the ECA at every time step during the degradation process is calculated for each computational node in CCL. This local ECA is used as input for the kinetic equation for ORR and for calculating the effective diffusion length[43] in the micro-scale oxygen transport resistance at each node in CCL for the M2 model.

Current cycling test scheme.—Intensive computation of physics-based comprehensive PEFC model, transient M2 model, is a great challenge. The time step to perform Pt degradation modeling is quite small compared with the time step of the M2 model. Thus, a dual-time-step approach is used in the current study as shown in Figure 3. The dual-time-step approach means a larger time step, Δt, is used for M2 model to accelerate the speed of computation and a smaller time step, δt, is used for Pt degradation submodel to capture the fast transients of Pt dissolution from small nanoparticles and Pt^{2+} redeposition to

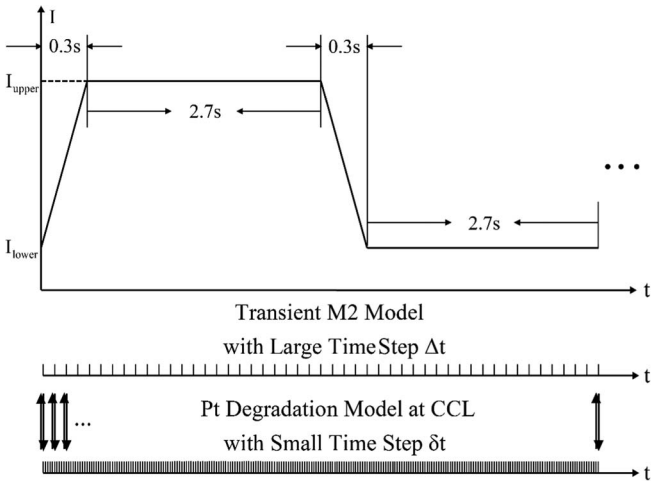

Figure 3. Illustration of current density profile and dual-time-step method.

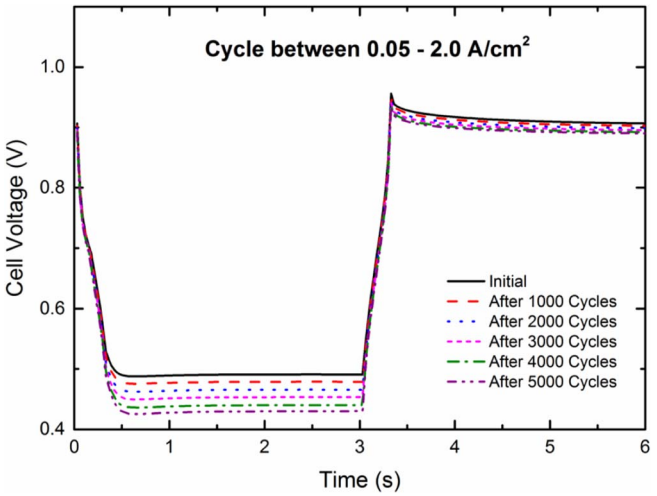

Figure 4. Voltage responses during current density cycling test between 0.05 and 2.0 A/cm^2.

large nanoparticles under various voltage conditions. The transient M2 model provides the temperature, humidity, electronic- and ionic-phase potential fields for the Pt degradation model, and the Pt degradation model returns the ECA at every time step for the transient M2 model. The current study models a total time of 5000 current cycles with 6s of each cycle. The current density profile in each voltage cycle is shown in Figure 3.

The steady state operation tests are also performed to characterize the performance of the pristine and cycled PEFCs. The steady state operations of the initial PEFC are first performed under a series of current density conditions. The current densities from 0.05 A/cm^2 to 2.0 A/cm^2 with step of 0.05 A/cm^2 are applied sequentially. Thus the polarization curve for the PEFC at the beginning of life can be generated. Then, after every 1000 current cycles until the end of current cycle test, the same parametric sweep of current densities is performed to generate the polarization curve for this degraded PEFC. At the same time, the remaining ECA distributions and reaction current density distributions in the pristine and cycled CCLs under those steady state operation testing conditions can be generated to specifically investigate the non-uniform Pt degradation and the shift of reaction current density in CCLs through degradation.

Results and Discussion

Overall performance loss due to Pt degradation.—For both the current cycling test and the steady characterization test, the PEFC is operated under 80°C and 150 kPa. The stoichiometry flow rate ratio is 1.5 for anode and 2.0 for cathode corresponding to 2.0 A/cm^2 in the cycling test, and the inlet humidity is kept at 65% at both anode and cathode inlet. For the PEFC catalyst electrodes, the anode Pt loading is 0.05 mg/cm^2, while the cathode Pt loading is 0.10 mg/cm^2 in this study. This low cathode loading is chosen to better investigate the interactions of the Pt degradation with the micro-scale oxygen transport resistance. Figure 4 shows the dynamic voltage response of the PEFC during the current density cycling test. It can be seen that the current cycling between high and low current densities causes a voltage cycling between low and high. This voltage cycling condition is similar to the potential cycle durability test condition which will accelerate Pt degradation. For the cycled PEFC, the loss of ECA causes loss of voltage as indicated in Figure 4, and this voltage deficiency is much larger under high current density condition.

The underlying reason can be clearly explained with the polarization curves of the cycled PEFC as shown in Figure 5. The current model predicts that the average ECA remaining in CCL after the 5000 cycle test is 66.2% of the ECA at beginning of life. Assuming Tafel kinetics for a simplified analysis,[7] the ORR kinetic voltage loss is roughly 12.5 mV. As indicated in Figure 5, the total voltage loss after 5000 cycle test is 28.1 mV under 1.0 A/cm^2. This demonstrates that the ORR kinetic loss and the micro-scale transport loss both contribute to the total voltage loss under moderate current condition. On the other hand, under the high current density condition, the micro-scale oxygen transport resistance is triggered by high ECA normalized current density and poses an additional interfacial concentration overpotential. Also, this micro-scale oxygen transport resistance is amplified by the ECA loss during Pt degradation process and causes larger interfacial concentration overpotential for the cycled PEFC. From Figure 5, it can be observed that the total voltage loss after 5000 cycle test is 70.6 mV under 2.0 A/cm^2, which is several times larger than the voltage loss predicted by ORR kinetics. This result suggests that the micro-scale transport resistance dominates the voltage loss for the degraded CCL under high current density, as the ECA loss substantially amplifies the micro-scale transport resistance. The voltage deficiency under large current density implies power deficiency for cycled PEFC when the power demand is high, which is highly undesirable. Therefore, quantitative estimation of the Pt degradation and the voltage loss of cycled PEFC is necessary and mitigation strategies to depress Pt degradation under dynamic load condition is warranted.

Non-uniform Pt degradation and ensuing current density distributions.—The Pt degradation in CCL is indeed highly

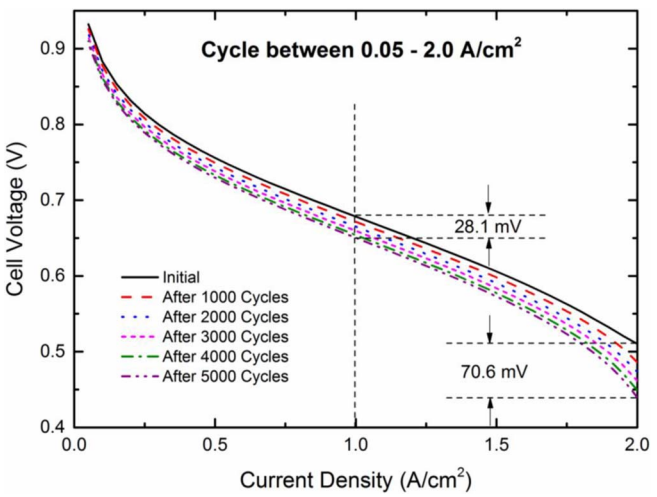

Figure 5. Polarization curves through current cycling test of 5000 cycles between 0.05 A/cm^2 – 2.0 A/cm^2.

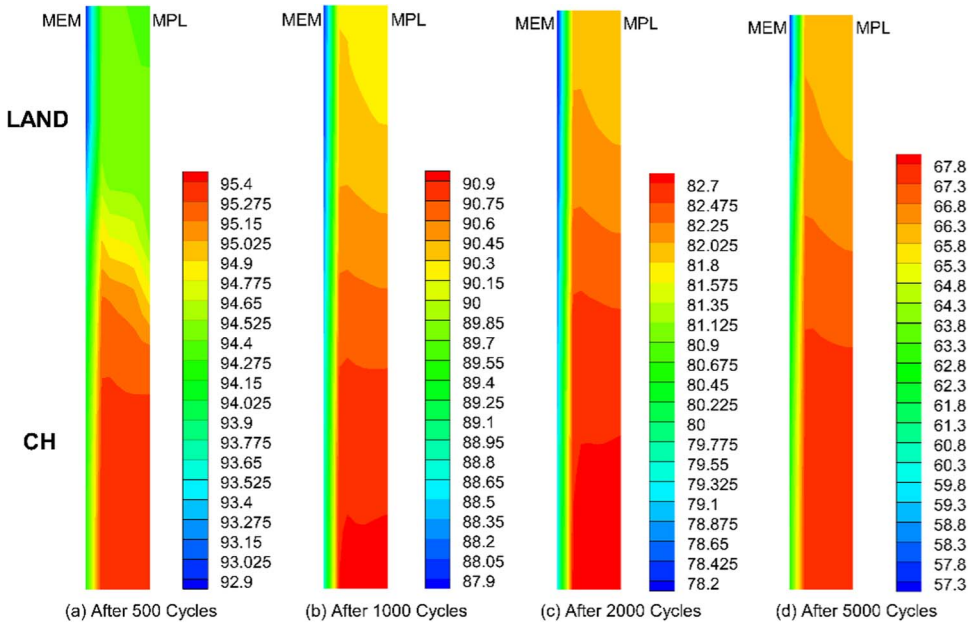

Figure 6. Normalized ECA remaining in CCL during 5000 cycles between 0.05 A/cm^2 – 2.0 A/cm^2.

non-uniform and the non-uniform ECA distribution after degradation is hard to estimate experimentally. The current study provides an effective method to estimate this non-uniform degradation and the consequence thereof. The remaining ECA distributions during the current cycling test are shown in Figure 6. The most significant non-uniform degradation is found in the through-plane direction and exacerbated Pt degradation can clearly be found near the CCL and membrane interface. In the CCL, the temperature is lower under the land due to shorter path of heat transfer, while the RH is higher under the land due to longer path of water transport. Lower temperature would cause slower Pt degradation and higher RH would cause faster Pt degradation. Thus, without appropriate method, it is hard to quantify the non-uniform Pt degradation in the channel-land direction. With the present modeling method, it is found that the degradation is faster under the land as shown in Figure 6. The non-uniformity of Pt degradation in the channel-land direction is observed to be slightly smaller than the non-uniformity of Pt degradation in the through-plane direction for this case. It is worthwhile to mention that the land and channel width in this study are both 0.5 mm, which is chosen to mimic the recent trend to reduce land width for oxygen transport enhancement and better water removal under the land. If the land width was 1.0 mm, the non-uniformity of Pt degradation in the channel-land direction would be higher due to longer path of water transport under the land. As shown in Figure 6, the difference of remained ECA under channel and land areas is less than 3%, indicating that the non-uniform Pt degradation along the in-plane direction is insignificant and hence there is little need to experimentally separate Pt degradation under land from channel areas, respectively.

Much attention has been paid on the local current density distributions in the PEFC CCLs in recent years.[43,57,65] The non-uniform Pt degradation would induce shift in the current density distributions in the cycled CCLs. Without a proper modeling method, estimation of the current density distribution in the CCL is hard. Figure 7 shows the local current density distribution in the initial and cycled CCL under the average current density of 1.0 A/cm^2, which represents a moderate current density condition. It can be found that the shift of current density distribution caused by the non-uniform ECA loss is mainly in the through-plane direction. This means that the non-uniform ECA loss in through-plane direction clearly shifts the current density distribution under moderate current density. However, as the magnitude of non-uniformity of ECA loss is relatively small in the channel-land direction, the shift of the current density distribution is not significant in this direction under moderate current density. On the other hand, as shown in Figure 8, the shift of current density distributions can be found in both through-plane and channel-land directions as the micro-scale oxygen transport resistance comes into effect under high current density PEFC operation. Lower ECA remains under the land in the cycled CCL and triggers higher micro-transport resistance. Thus, the reaction current density under the land is lower for the cycled CCL under high current density condition. It is worth noticing that the current study investigates the CCL with Pt loading of 0.1 mg/cm^2. When the CCL Pt loading is further lowered, this micro-scale resistance induced current density non-uniformity would be further amplified as this micro-scale resistance is inversely proportional to ECA.

Effects of raising lower current density and operating temperature.—Lowering the upper voltage is an effective approach to alleviate the aggressive Pt degradation in PEFC CCLs. As for the realistic automotive PEFCs working under highly dynamic load condition, raising the lower current density the PEFCs provide should be an effective mitigation approach for Pt degradation. This limitation of lower current density can be achieved by co-operation of PEFC with another power source, for example, a battery. The PEFC could work under more steady condition by depositing energy into the battery when the power need is low and using the deposited energy when the power need is high. The current study specifically investigates the effect of raising the lower current density under current density cycling condition. The I_{upper} is fixed at 2.0 A/cm^2, and the I_{lower} is raised from 0.05 A/cm^2 to 0.10 A/cm^2, while other operating conditions are kept to be identical.

The dynamic voltage response profiles during the 5000 cycle test are shown in Figure 9. It could be found that the upper voltage is effectively reduced by raising the lower current density in the cycling. The overall ECA evolutions are shown and compared in Figure 10. The overall ECA remaining after 5000 cycle test is improved from 66.2% to 78.9% with lower current density raised from 0.05 A/cm^2 to 0.10 A/cm^2. Clearly, raising the lower current density could depress ECA loss through lowering the upper voltage. Figure 11 compares the polarization curves after 5000 cycles under different I_{lower}. It is observed that by increasing the I_{lower}, the performance loss of PEFC is clearly reduced. The voltage loss at 1.0 A/cm^2 is reduced from 28.1 mV to 16.0 mV, while the voltage loss at 2.0 A/cm^2 is reduced from 70.6 mV to 41.4 mV by raising the lower current density from 0.05 A/cm^2 to 0.10 A/cm^2. The non-uniform Pt degradation with I_{lower}

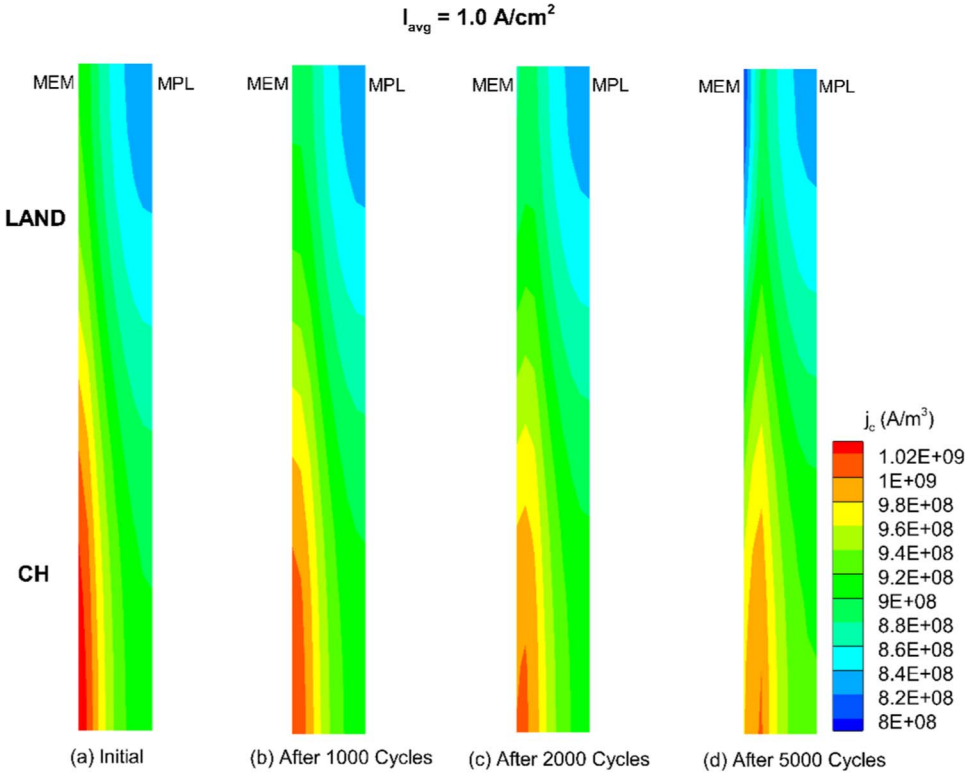

Figure 7. Local current density distribution in cycled CCL under average current density of 1.0 A/cm^2.

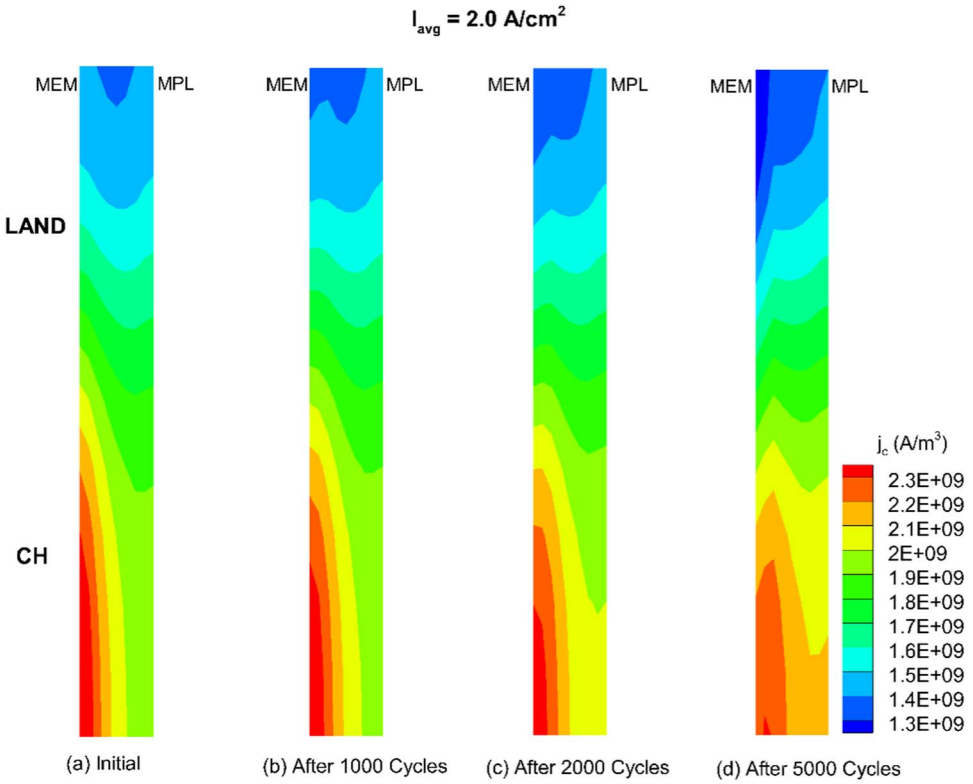

Figure 8. Local current density distribution in cycled CCL under average current density of 2.0 A/cm^2.

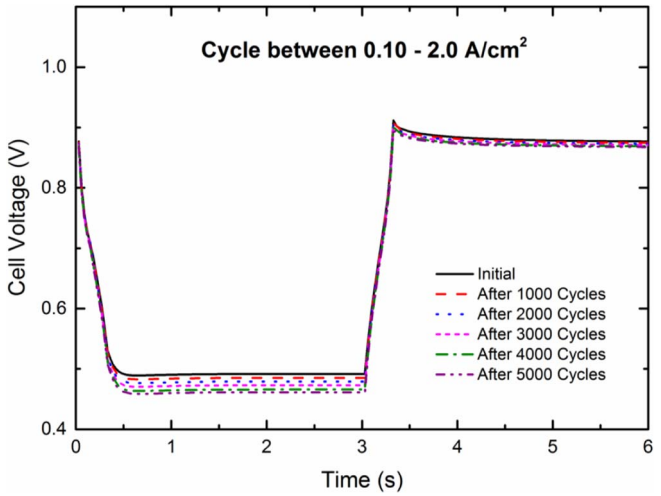

Figure 9. Voltage responses during current density cycling test between 0.10 and 2.0 A/cm^2.

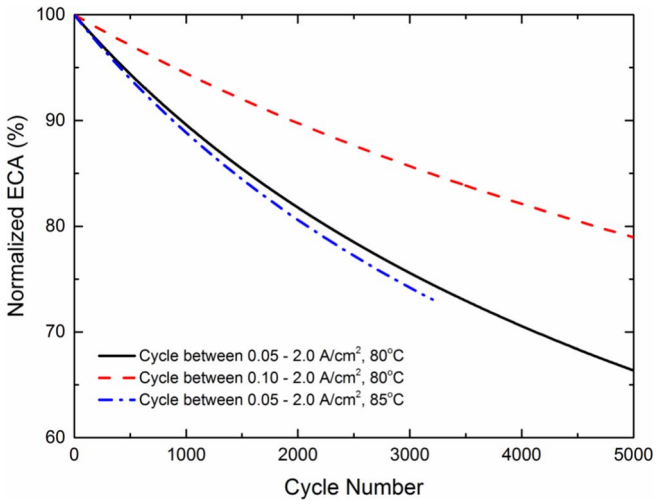

Figure 10. Overall normalized ECA evolutions during current density cycling test.

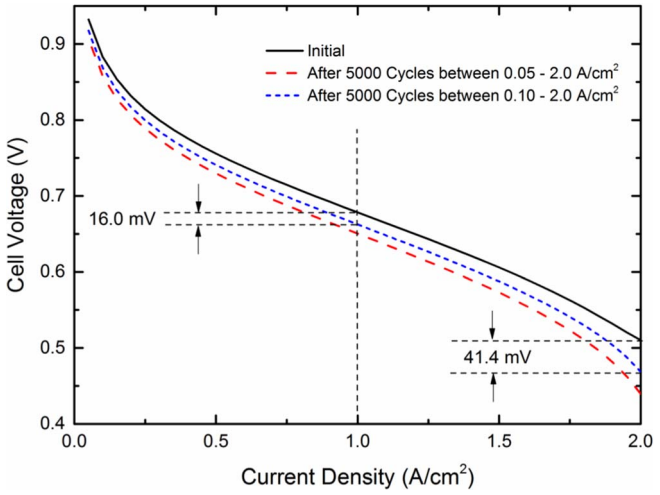

Figure 11. Polarization curves comparison after whole cycling tests under various current cycling profiles.

of 0.10 A/cm^2 is shown in Figure 12. Although the non-uniformity of ECA loss in both through-plane and channel-land directions can still be seen, the remaining ECA in CCL is higher than the ECA left under I_{lower} of 0.05 A/cm^2 at every position. The implication is that raising the lower current density the PEFC supplies could alleviate the ECA loss at every position in the entire CCL. This means for realistic automotive PEFCs, limiting the lower current under dynamic load condition has significance benefit in extending the lifetime of PEFCs.

Then, the effect of higher temperature operation on the PEFC Pt degradation is investigated. The operating temperature during the current cycling test (0.05–2.0 A/cm^2) and voltage characterization is raised from 80 to 85°C while the other conditions are kept the same. As shown in Figure 10, the overall ECA loss increases slightly with the increasing temperature. Figure 13 shows the polarization curves of the pristine and cycled cells under the higher operating temperature and it is found that the ohmic losses for both initial and aged cells increase as the operating temperature is raised. The higher operating temperature of PEFC causes higher temperature in CCL which accelerates Pt degradation while reduces the humidity in CCL which decelerates Pt degradation. These opposite effects[55] are both

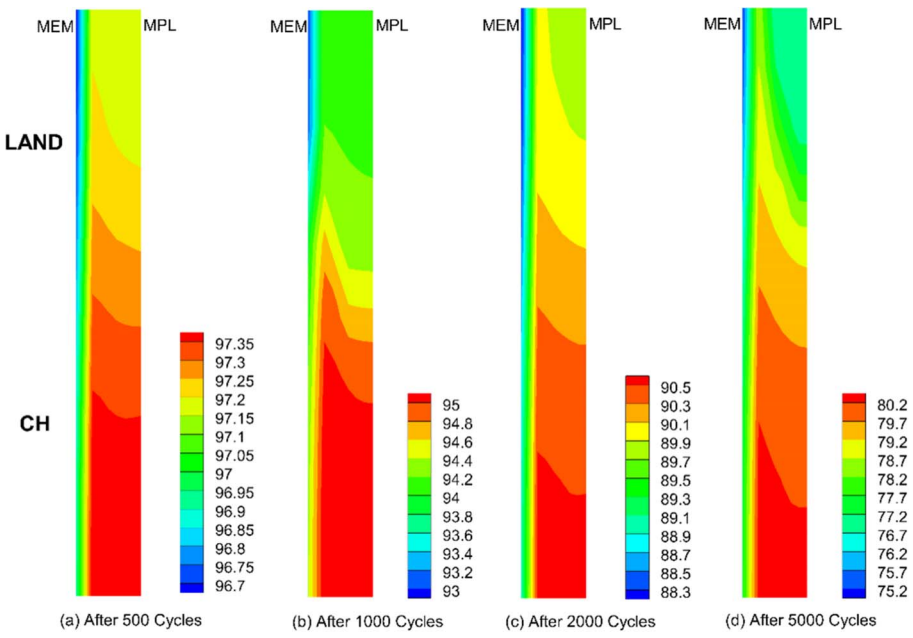

Figure 12. Normalized ECA remaining in CCL during 5000 cycles between 0.10 A/cm^2–2.0 A/cm^2.

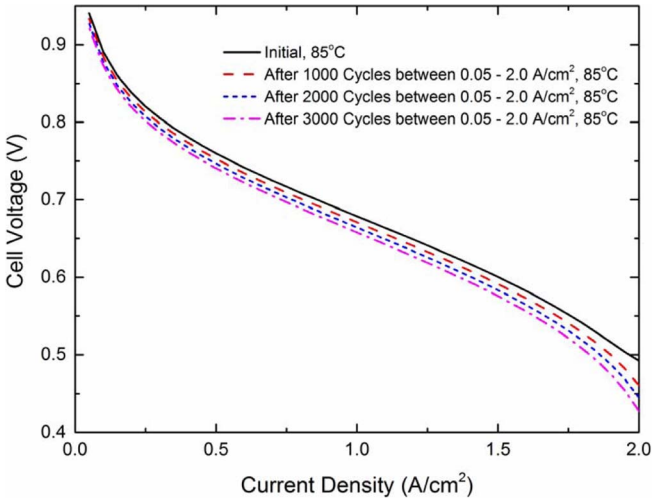

Figure 13. Polarization curves in current cycling tests under higher operating temperature.

captured by the physics-based Pt degradation model in combination with M2 performance model and the net effect on Pt degradation is given.

Conclusions

The interactions of Pt degradation and the performance loss of a low Pt-loading PEFC are investigated with a transient Pt degradation model developed in this work. First, the overall performance loss through a 5000 current cycling test is quantitatively predicted and analyzed. It is found for the cycled PEFC under high current density, the micro-scale transport resistance is amplified by Pt degradation induced ECA loss and dominates the total voltage loss. Second, the present model predicts that Pt degradation is non-uniform in both through-plane and channel-land directions in PEFC CCL. Under high current density, a shift of the local current density in the channel-land direction is observed as the low ECA left under the land caused by high humidity amplifies the micro-scale oxygen transport resistance at this region. Nonetheless, the in-plane non-uniformity of Pt degradation between land and channel areas remains less than 3%, suggesting little need to experimentally look into the separate characterization of Pt degradation along the in-plane direction. Third, the strategy of raising the lower current density is tested with the Pt degradation model. The performance loss, overall ECA loss and local ECA loss are all found to be effectively alleviated by this method. To sum up, the transient Pt degradation modeling offers a useful method to analyze the cause of Pt degradation distribution and forecast its significance, which is valuable to achieve the goal of longer lifespan and better lifetime performance for low Pt-loading PEFCs.

List of Symbols

a	water activity
C^k	molar concentration of species k, mol/m^3
c_p	specific heat, J/kg K
$c_{Pt^{2+}}$	Pt^{2+} concentration, mol/m^3
$c^{ref}_{Pt^{2+}}$	reference Pt^{2+} concentration, mol/m^3
D	species diffusivity, m^2/s
d	Pt particle diameter, m
F	Faraday's constant, 96,487 C/equivalent
$\bar{H}_{1,fit}$	Pt dissolution activation energy, J/mol
$\bar{H}_{1,fit,100\%RH}$	Pt dissolution activation enthalpy under fully humidified condition, J/mol
$\overline{H}_{2,fit}$	Partial molar oxide formation activation enthalpy (zero coverage), J/mol
$\vec{j}_l$	mass flux of liquid phase, kg/m^2 s
k	thermal conductivity, W/m K
M	molecular weight, kg/mol
mf_l^k	mass fraction of species k in liquid phase
n	number of electrons transferred
P	pressure, Pa
R	universal gas constant, 8.314 J/mol K
$r_{net,oxide}$	Pt particle net oxidation rate, mol/m^2 s
$r_{net,Pt}$	Pt particle dissolution rate, mol/m^2 s
S	source term in transport equations
T	temperature, K
t	time, s
U_{fit}	Pt oxide formation bulk equilibrium voltage, V
U_{eq}	Pt dissolution bulk equilibrium voltage, V
$\vec{u}$	velocity vector, m/s

Greek

β_1	Butler-Volmer transfer coefficient for Pt dissolution
β_2	Butler-Volmer transfer coefficient for Pt oxide formation
Γ	Pt surface site density, mol/m^2
γ_c	correction factor for species convection
γ_T	correction factor for thermal convection
γ_{total}	total surface tension, J/m^2
ε	porosity
θ	Pt fractional oxide coverage
κ	ionic conductivity, S/m
μ	viscosity, kg/m^3
Λ	Pt oxide dependent kinetic barrier constant, J/mol
ν_1	dissolution attempt frequency, Hz
ν_2	backward dissolution rate factor, Hz
ν_1^*	forward Pt oxide formation rate constant, Hz
ν_2^*	backward Pt oxide formation rate constant, Hz
ρ	density, kg/m^3
σ	electronic conductivity, S/m
τ	shear stress, N/m^2
Φ	phase potential, V
Ω	molar volume of Pt, m^3/mol
ω	Pt oxide-oxide interaction energy, J/mol

Superscript and Subscripts

e	Electrolyte
eff	effective value
g	gas phase
k	Species
ref	Reference
s	Solid

References

1. R. Borup, J. Meyers, B. Pivovar, Y. S. Kim, R. Mukundan, N. Garland, D. Myers, M. Wilson, F. Garzon, D. Wood, P. Zelenay, K. More, K. Stroh, T. Zawodzinski, J. Boncella, J. E. McGrath, M. Inaba, K. Miyatake, M. Hori, K. Ota, Z. Ogumi, S. Miyata, A. Nishikata, Z. Siroma, Y. Uchimoto, K. Yasuda, K. I. Kimijima, and N. Iwashita, *Chem. Rev.*, **107**, 3904 (2007).
2. N. Nonoyama, S. Okazaki, A. Z. Weber, Y. Ikogi, and T. Yoshida, *J. Electrochem. Soc*, **158**, B416 (2011).
3. A. Ohma, T. Mashio, K. Sato, H. Iden, Y. Ono, K. Sakai, K. Akizuki, S. Takaichi, and K. Shinohara, *Electrochim. Acta*, **56**, 10832 (2011).
4. W. Yoon and A. Z. Weber, *J. Electrochem. Soc*, **158**, B1007 (2011).
5. T. A. Greszler, D. Caulk, and P. Sinha, *J. Electrochem. Soc*, **159**, F831 (2012).
6. J. P. Owejan, J. E. Owejan, and W. Gu, *J. Electrochem. Soc*, **160**, F824 (2013).
7. P. Zihrul, I. Hartung, S. Kirsch, G. Huebner, F. Hasché, and H. A. Gasteiger, *J. Electrochem. Soc*, **163**, 492 (2016).
8. H. A. Gasteiger, J. E. Panels, and S. G. Yan, *J. Power Sources*, **127**,162 (2004).
9. M. Uchimura and S. Kocha, *ECS Trans*., **11** (1), 1215 (2007).
10. M. Uchimura, S. Sugawara, Y. Suzuki, J. Zhang, and S. Kocha, *ECS Trans*., **16** (2), 225 (2008).
11. A. Ohma, K. Shinohara, A. Liyama, T. Yoshida, and A. Daimaru, *ECS Trans*., **41** (1), 775 (2011).

12. E. F. Holby, W. Sheng, Y. Shao-Horn, and D. Morgan, *Energy Environ. Sci.*, **2**, 865 (2009).
13. P.J. Ferreira, G.J. la O', Y. Shao-Horn, D. Morgan, R. Makharia, S. Kocha, and H.A. Gasteiger, *J. Electrochem. Soc*, **152**, A2256 (2005).
14. A. A. Topalov, I. Katsounaros, M. Auinger, S. Cherevko, J. C. Meier, S. O. Klemm, and K. J. J. Mayrhofer, *Angew. Chem. Int. Ed.*, **51**, 12613 (2012).
15. K. Ono, Y. Yasuda, K. Sekizawa, N. Takeuchi, T. Yoshida, and M. Sudoh, *Electrochim. Acta*, **97**, 58 (2013).
16. T. Nagai, H. Murata, and Y. Morimoto, *J. Electrochem. Soc*, **161**, F789 (2014).
17. P. Urchaga, T. Kadyk, S. G. Rinaldo, A. O. Pistono, J. Hu, W. Lee, C. Richards, M. H. Eikerling, and C. A. Rice, *Electrochim. Acta*, **176**, 1500 (2015).
18. J. A. Gilbert, N. N. Kariuki, X. Wang, A. J. Kropf, K. Yu, D. J. Groom, P. J. Ferreira, D. Morgan, and D. J. Myers, *Electrochim. Acta*, **173**, 223 (2015).
19. M. Eikerling, K. Malek, and Q. Wang, in *PEM Fuel Cell Electrocatalysts and Catalyst Layers: fundamentals and applications*, J. Zhang, Editor, p. 381, Springer, London (2008).
20. A. Z. Weber, R. L. Borup, R. M. Darling, P. K. Das, T. J. Dursch, W. Gu, D. Harvey, A. Kusoglu, S. Lister, M. M. Mench, R. Mukundan, J. P. Owejan, J. G. Pharoah, M. Secanell, and I. V. Zenyuk, *J. Electrochem. Soc*, **161**, F1254 (2014).
21. T. E. Springer, M. S. Wilson, and S. Gottesfeld, *J. Electrochem. Soc*, **140**, 3513 (1993).
22. M. Eikerling and A. A. Kornyshev, *J. Electroanal. Chem.*, **453**, 89 (1998).
23. K. Broka and P. Ekdunge, *J. Appl. Electrochem.*, **27**, 281 (1997).
24. N. P. Siegel, M. W. Ellis, D. J. Nelson, and M. R. von Spakovsky, *J. Power Sources*, **115**, 81 (2003).
25. Q. Wang, D. Song, T. Navessin, S. Holdcroft, and Z. Liu, *Electrochim. Acta*, **50**, 725 (2004).
26. W. Sun, B. A. Peppley, and K. Karan, *Electrochim. Acta*, **50**, 3359 (2005).
27. P. K. Das, X. Li, and Z.-S. Liu, *J. Power Sources*, **179**, 186 (2008).
28. J. Liu and M. Eikerling, *Electrochim. Acta*, **53**, 4435 (2008).
29. S. Um, C. Y. Wang, and K. S. Chen, *J. Electrochem. Soc*, **147**, 4485 (2000).
30. T. Berning and N. Djilali, *J. Electrochem. Soc*, **150**, A1589 (2003).
31. G. Lin, W. He, and T. V. Nguyen, *J. Electrochem. Soc*, **151**, A1999 (2004).
32. A. Weber and J. Newman, *Chem. Rev.*, **104**, 4679 (2004).
33. C. Y. Wang, *Chem. Rev.*, **104**, 4727 (2004).
34. P. T. Nguyen, T. Berning, and N. Djilali, *J. Power Sources*, **130**, 149 (2004).
35. Y. Wang and C. Y. Wang, *J. Power Sources*, **153**, 130 (2006).
36. S. Shimpalee, D. Spuckler, and J. W. van Zee, *J. Power Sources*, **167**, 130 (2007).
37. L. Hao, K. Moriyama, W. Gu, and C. Y. Wang, *J. Electrochem. Soc*, **163**, F744 (2016).
38. G. Wang, P. P. Mukherjee, and C. Y. Wang, *Electrochim. Acta*, **51**, 3139 (2006).
39. G. Wang, P. P. Mukherjee, and C. Y. Wang, *Electrochim. Acta*, **52**, 6367 (2007).
40. K. J. Lange, P.-C. Sui, and N. Djilali, *J. Electrochem. Soc*, **157**, B1434 (2010).
41. K. J. Lange, P.-C. Sui, and N. Djilali, *J. Power Sources*, **196**, 3195 (2011).
42. P. P. Mukherjee and C. Y. Wang, *J. Electrochem. Soc*, **153**, A840 (2006).
43. L. Hao, K. Moriyama, W. Gu, and C. Y. Wang, *J. Electrochem. Soc*, **162**, F854 (2015).
44. R. M. Darling and J. P. Meyers, *J. Electrochem. Soc*, **150**, A1523 (2003).
45. R. M. Darling and J. P Meyers, *J. Electrochem. Soc*, **152**, A242 (2005).
46. A. A. Franco and M. Tembely, *J. Electrochem. Soc*, **154**, B712 (2007).
47. W. Bi and T. F. Fuller, *J. Power Sources*, **178**, 188 (2008).
48. T. Takeshita, M. Murata, T. Hatanaka, and Y. Morimoto, *ECS Trans.*, **16** (2), 367 (2008).
49. S. G. Rinaldo, J. Stumper, and M. Eikerling, *J. Phys. Chem. C*, **114**, 5773 (2010).
50. E. F. Holby and D. Morgan, *J. Electrochem. Soc*, **159**, B578 (2012).
51. R. K. Ahluwalia, S. Arisetty, X. Wang, X. Wang, R. Subbaraman, S. C. Ball, S. DeCrane, and D. J. Myers, *J. Electrochem. Soc*, **160**, F447 (2013).
52. R. K. Ahluwalia, S. Arisetty, J.-K. Peng, R. Subbaraman, X. Wang, N. Kariuki, D. J. Myers, R. Mukundan, R. Borup, and O. Polevaya, *J. Electrochem. Soc*, **3**, F291 (2014).
53. Y. Li, K. Moriyama, W. Gu, S. Arisetty, and C. Y. Wang, *J. Electrochem. Soc*, **162**, F834 (2015).
54. T. Takeshita, H. Murata, T. Hatanaka, and Y. Morimoto, *ECS Trans.*, **16** (2), 367 (2008).
55. Y. Morimoto and S. Yamakawa, in *Polymer Electrolyte Fuel Cell Degradation*, M. M. Mench, E. C. Kumbur, and T. N. Veziroglu, Editors, p. 423, Academic Press, Boston (2012).
56. M. Gerard, C. Robin, M. Chandesris, and P. Schott, *ECS Trans.*, **75** (14), 35 (2016).
57. S. Jomori, N. Nonoyama, and T. Yoshida, *J. Power Sources*, **215**, 18 (2012).
58. S. S. Kocha, in *Polymer Electrolyte Fuel Cell Degradation*, M. M. Mench, E. C. Kumbur, and T. N. Veziroglu, Editors, p. 89, Academic Press, Boston (2012).
59. S. Basu, C. Y. Wang, and K. S. Chen, *J. Electrochem. Soc*, **156**, B748 (2009).
60. H. A. Gasteiger, S. S. Kocha, B. Sompalli, and F. T. Wagner, *Appl. Catal., B*, **56**, 9 (2005).
61. M. K. Debe, *Nature*, **486**, 43 (2012).
62. Y. J. Wang, N. Zhao, B. Fang, H. Li, X. T. Bi, and H. Wang, *Chem. Rev.*, **115**, 3433 (2015).
63. M. Shao, Chang Q, J. P. Dodelet, and R. Chenitz, *Chem. Rev.*, **116**, 3594 (2016).
64. Y. Wang and C.Y. Wang, *J. Electrochem. Soc*, **153**, A1193 (2006).
65. Y. Wang and X. Feng, *J. Electrochem. Soc*, **155**, B1289 (2008).